WEP Warwick Evans Publishing

International Journal of Natural Resources and Environmental Studies

ISSN: 3006-2012 (Print), ISSN: 3006-0834 (Online) | Volume 6, Number 1, Year 2025
DOI: https://doi.org/10.62051/ijnres.v6n1.11
Journal homepage: https://wepub.org/index.php/IJNRES/index

Extraction of 3D Displacement of Mining Area Surface Based on Multi-Source Data Fusion

Jiankun Han*

School of Surveying and Land Information Engineering, Henan Polytechnic University, Jiaozuo, Henan 454003, China

*Corresponding Author: Jiankun Han (212204010036@home.hpu.edu.cn)

ABSTRACT

Large-scale, continuous, and high-intensity mining of underground coal resources in mining areas often leads to large-scale surface subsidence, sometimes up to several meters. The use of InSAR to monitor subsidence usually faces two key challenges: rapid and large-gradient subsidence often leads to image decorrelation, which hinders the acquisition of accurate deformation measurements. In addition, InSAR-based monitoring is limited to one-dimensional line-of-sight (LOS) displacement, which limits its ability to fully capture three-dimensional surface deformation. To overcome these obstacles, this study combines InSAR and PIM technology, and uses a spatial interpolation method to obtain continuous surface subsidence data in a geographic coordinate system to generate a surface displacement basin map in the mining area. A three-dimensional displacement model was established based on the proportional relationship between horizontal surface movement caused by mining of inclined coal seams and surface inclination. A field test was carried out in Yangchangwan Coal Mine, and the method was applied and its accuracy analyzed using five Sentinel-1A images from October 2022 to January 2023, combined with leveling data. The experimental results show that this method can obtain surface subsidence information around the mining area more accurately, the overall subsidence situation is more consistent with the actual situation, and the monitoring capability is significantly improved compared with InSAR and PIM.

KEYWORDS

InSAR; Probability Integral Method(PIM); Mining subsidence; Large gradient deformation; Three-dimensional displacement.

1. INTRODUCTION

Coal remains China's primary energy source and a crucial industrial material, accounting for 55.3% of the nation's energy mix in 2023 [1]. Surface subsidence during coal mining causes various hazards and safety concerns. Statistics indicate that over 1 million hectares of land in China have been damaged by mining-induced subsidence, with an additional 70,000 hectares affected each year. This extensive surface damage has severely degraded the ecological environment in mining areas, posed threats to infrastructure and buildings [2,3], and worsened living conditions for residents. To mitigate these issues, it is critical to accurately capture surface deformation data [4,5].

At present, the acquisition of surface deformation information primarily relies on traditional monitoring methods. Typically, two observation lines are arranged along the working face, and traditional point measurement methods, such as leveling and RTK, are used to monitor subsidence and horizontal displacement at various points along these lines. While these methods offer high point accuracy, their coverage is limited, measurement frequency is constrained, and measurement points

are prone to damage, making it challenging to effectively capture three-dimensional deformations [6]. With advancements in surveying technology, surface mapping techniques such as 3D laser scanning, unmanned aerial vehicles (UAVs), and SAR have been developed. Among these surface mapping technologies, DInSAR is currently widely used for monitoring small-gradient deformations.

Compared to traditional techniques, DInSAR offers all-weather, all-time monitoring capabilities with extensive spatial coverage, while reducing labor intensity and costs. The surface subsidence in the Daliuta coal mining area in China is generally measured in meters, which is typical of large-gradient deformation [7,8]. However, there are limitations of InSAR in deformation monitoring in mines[9]. These limitations are primarily manifested in the following aspects: (1) SAR images lose coherence due to large-gradient surface deformation caused by mining, often leading to phase unwrapping failures and consequently inaccurate results [10]. (2) SAR can only monitor surface deformation in one dimension, whereas the actual deformation caused by mining is three-dimensional [11,15]. To address these issues, many researchers have explored various methods, which can be categorized into three types: (I) Multi-track InSAR [16,18], InSAR combined with displacement tracking/MAI [19,21], and InSAR combined with GPS [22,24]; (II) Prior models combined with InSAR [25,27]; (III) InSAR combined with the PIM [28,30].

Method (I). Theoretically, the amalgamation of one-dimensional or two-dimensional observations from various directions can enhance the quantity of observational Eqs. Thus enhancing the ability to supplement and reconstruct comprehensive three-dimensional displacement data. Additionally, displacement tracking technology can to some extent capture large-gradient deformations caused by mining. However, in practice, this method faces constraints such as the number of SAR images and low image resolution.

Method (II). By constructing additional constraints based on a priori 3D displacement relations, 3D displacements can be extracted from InSAR observations. In contrast to Method (I), Method (II) exhibits a reduced dependency on observational data and significantly improves the accuracy of displacement estimations, especially in the north-south direction. However, it is mainly limited by the reliance on the reliability of the a priori model and is unable to extract large-gradient 3D deformations.

Method (III). This method partially addresses the issue of phase loss in InSAR technology when monitoring large-gradient deformations in mining areas (i.e., the limitations of Methods (I) and (II)). This method requires only single-track SAR images and does not necessitate additional auxiliary observational data, offering high cost-effectiveness. Therefore, this study employs the third method for extracting three-dimensional deformations. However, when combining InSAR monitoring results with PIM predictions, discontinuities and non-smooth transitions often occur at the junctions.

For this reason, this paper proposes an integrated method combining InSAR, the Probability Integral Method (PIM), and a log-logistic model to extract large-gradient 3D deformations. First, the cumulative subsidence basin from the InSAR time series is calculated, and constraints are established to differentiate between the subsidence edges and centers of large-gradient deformations. In cases of slight deformation at the subsidence edges, the InSAR results are retained. For large-gradient subsidence centers, a subsidence basin model is developed by integrating InSAR with PIM. Subsequently, Kriging interpolation is used to obtain continuous surface subsidence information. To mitigate the discontinuities at the edges, a weighted fusion approach is employed to derive comprehensive subsidence information. Finally, the proportional relationship between horizontal movement and surface tilt in PIM, combined with the log-logistic model, this method is employed to derive three-dimensional displacement in mining area. The specific flow is shown in Figure 1.

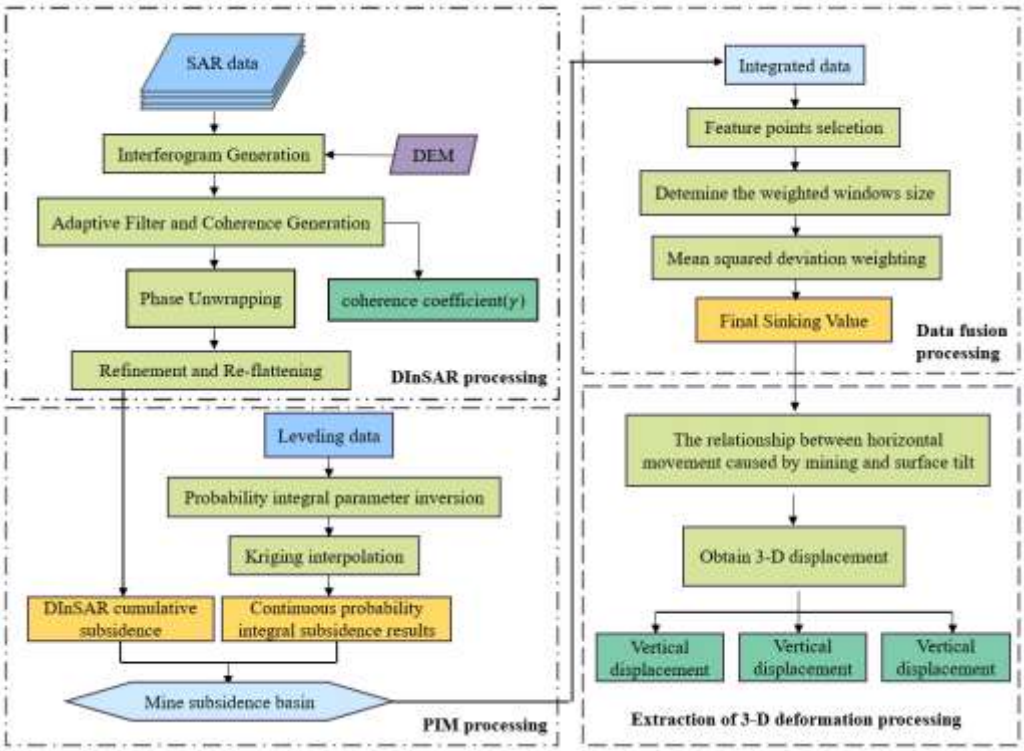

Figure 1. Technical process.

2. STUDY AREA AND DATA SOURCES

2.1. Study area

Yangchangwan Coal Mine is in Ningdong Coal Field in Yinchuan City, Ningxia Hui Autonomous Region. The mine is situated on the southwestern edge of the Maowusu Desert, and the geomorphological type is primarily wind-formed, consisting of deserts and grasslands, classified as a grassland desert zone. Most of the area in the wellfield is covered by mobile sand dunes, with sparse vegetation on the surface, and the terrain is generally low and flat with minimal undulation. The highest elevation of the wellfield is 1502 meters altitude, located in southern hill area, while the lowest elevation is 1395 meters. The terrain elevation generally ranges between 1410 and 1470 meters. In this study, the 120101 working face of the Yangchangwan coal mine was chosen as research area, which is 195 meters wide and 2900 meters long, with an average mining depth of about 355 meters and an average daily advance rate of approximately 8 meters.

2.2. Study Data

2.2.1. SAR Data

It provides continuous imaging under various weather conditions and is used for terrain mapping and surface deformation monitoring. Sentinel-1A has a revisit period of 12 days, and its orbital information is corrected using precise orbit data (AUX_POEORB). The study uses five Sentinel-1A images acquired between November 10, 2022, and January 9, 2023. Based on the temporal order of acquisition, resulting in four interferometric pairs.

2.2.2. Level Data

The South DL-2007 digital level from China Southern Company was used for third-order leveling measurements, with a monitoring accuracy of 1 mm. Subsidence data were obtained by deploying monitoring points in coal mining subsidence areas and conducting regular leveling surveys to record

changes in the height of the monitoring points over time. At Yangchangwan Coal Mine, 26 measurement points were strategically positioned along the strike of the working face, spaced at 30-meter intervals, spanning a total length of 780 meters, and 29 points were arranged along the dip direction at 30-meter intervals, spanning a total length of 900 meters. Leveling data were obtained through periodic measurements of the arranged points. The distribution of points is shown in Figure 2.

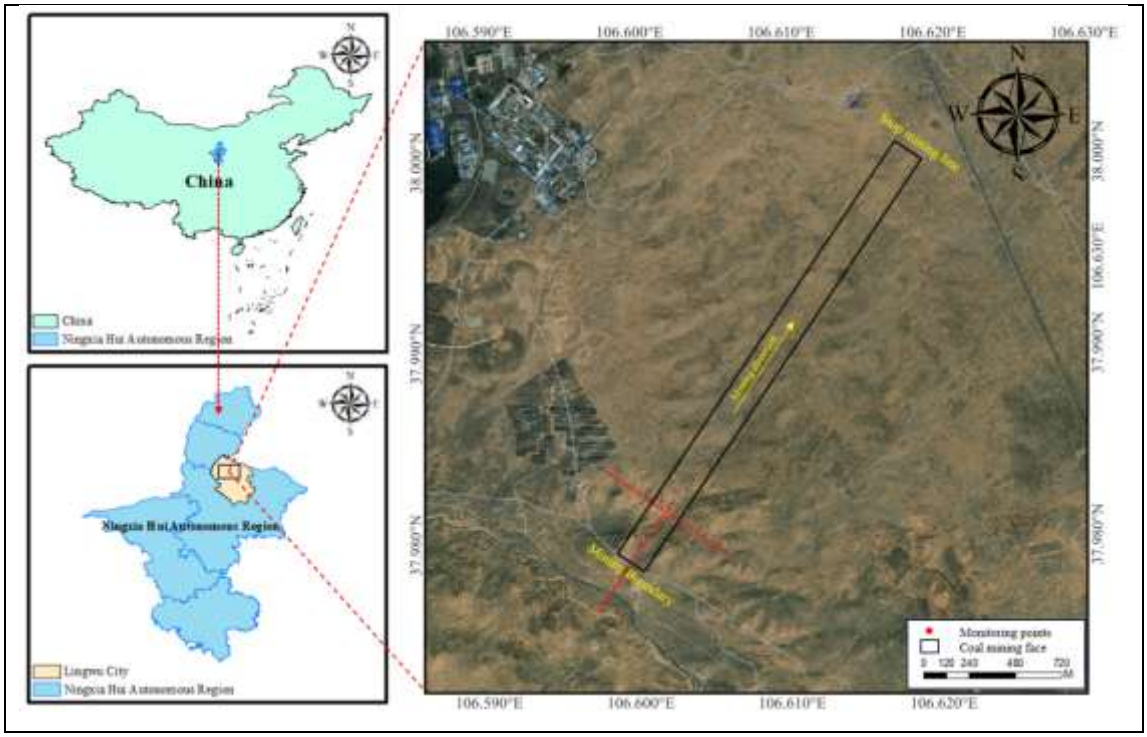

Figure 2. Study area.

3. RESEARCH METHODS

3.1. InSAR Technology and PIM Basic Theory

The InSAR technique obtains the interferometric phase φ by conjugate multiplication of two SAR images covering same region, expressed as Eq. (1). The phase information primarily includes: flat earth phase φ_{flat}, topographic phase φ_{topo}, surface deformation phase φ_{def}, atmospheric phase φ_{atm} caused by ionospheric and tropospheric delays, and noise phase φ_{noise}.

$$\varphi = \varphi_{\text{flat}} + \varphi_{topo} + \varphi_{def} + \varphi_{orbit} + \varphi_{atm} + \varphi_{noise} \quad (1)$$

After removing various interferences, the deformation phase appears as a series of interference fringes in the interferometric image. These interference fringes represent the relative phases between pixels. Based on this, Massonnet and Feigl [31] introduced the concept of deformation gradient to represent the relative displacement between any two points and defined the maximum deformation gradient that InSAR technology can monitor.

$$d_{max} = \frac{\lambda}{2\mu} \quad (2)$$

In the formula, d_{max} represents the maximum deformation gradient theoretically detectable by InSAR, μ denotes the size of a single SAR pixel, and λ is the radar wavelength. According to Eq. (2), d_{max} is theoretically closely related to radar parameters; a longer radar wavelength and a smaller pixel size allow for the detection of larger deformation gradients. For example, using C-band Sentinel

data processed with a 1:4 multi-look ratio (resolution of 20 meters), the theoretically detectable deformation gradient is 1.4 mm.

Eq. (2) is derived under ideal conditions. However, the deformation values monitored by InSAR is affected by factors such as orbital errors, which results in the actual monitored values usually being smaller than the theoretical values. To address this issue, Baran [32] investigated the impact of coherence on InSAR deformation gradient monitoring and proposed a threshold expression for the deformation gradient based on image coherence.

$$D_{max} = d_{max} + 0.002(\gamma - 1) \tag{3}$$

Eq. (3), D_{max} is the actual maximum monitorable deformation gradient of InSAR and γ is the image coherence coefficient. The larger the image coherence coefficient, the greater the maximum deformation gradient that InSAR can monitor. For SAR images, there exists a coherence coefficient threshold below which $D_{max} = 0$, meaning that surface deformation cannot be monitored. For example, for Sentinel images, when the coherence coefficient γ is 0.3, $D_{max} = 0$, indicating that surface deformation cannot be monitored when the coherence coefficient of Sentinel data falls below 0.3. In mining areas, due to the large deformation rates over short periods, the requirements for InSAR coherence are higher. In some areas with large deformation gradients, InSAR directly loses its monitoring capability. Therefore, in areas where InSAR cannot monitor surface deformation, the PIM can be used for analysis.

PIM is a method for forecasting surface subsidence based on the principles of stochastic media theory. This method is based on several assumptions: Assumption 1: The rock mass is assumed to be isotropic, homogeneous, and discontinuous, meaning that the surface movement caused by mining is direction-independent; this assumption is also known as the principle of equal influence. Assumption 2: The principle of linear superposition applies. Assumption 3: Within the curvature zone, the rock mass undergoes deformation without volume change. Assumption 4: As time approaches infinity, the volume of surface subsidence after stabilization equals the volume extracted. Based on these assumptions, the method treats the movement of the mine rock layers as a normally distributed random phenomenon and uses a probability density function to model the contours of the surface subsidence basin. According to the PIM theory, for the working face with strike length D_3 and dip length D_1, The subsidence of the point (x, y) is

$$W(x,y) = \frac{1}{W_0} W^0(x) W^0(y) \tag{4}$$

$$W^0(x) = \frac{W_0}{2}\left\{\frac{2}{\sqrt{\pi}}\int_0^{\sqrt{\pi}\frac{x\tan\beta}{H_0}} e^{-u^2}\,du - \frac{2}{\sqrt{\pi}}\int_0^{\sqrt{\pi}\frac{[x-(D_3-S_3-S_4)]\tan\beta}{H_0}} e^{-u^2}du\right\} \tag{5}$$

$$W^0(y) = \frac{W_0}{2}\left\{\frac{2}{\sqrt{\pi}}\int_0^{\sqrt{\pi}\frac{y\tan\beta_1}{H_1}} e^{-u^2}\,du - \frac{2}{\sqrt{\pi}}\int_0^{\sqrt{\pi}\frac{\left[y-(D_1-S_1-S_2)\frac{\sin(\theta+\alpha)}{\sin\theta}\right]\tan\beta_2}{H_3}} e^{-u^2}du\right\} \tag{6}$$

$$W_0 = m * q * \cos\alpha \tag{7}$$

In the working face coordinate system, W_0 represents the maximum subsidence value, and $W^0(x)$ and $W^0(y)$ represent the subsidence values of the projected points of the strike and dip (see Figure. 3(a)). u represents the mining unit for probability integration, and m denotes the coal seam thickness (see Figure 3(b)). H_0 is the average mining depth(see Figure 3(a)), and H_1 and H_3 represent the downhill and uphill mining depths(see Figure 3(c)). The parameter q is the subsidence coefficient, $\tan\beta$ is the tangent value of the main influence angle, $\tan\beta_1$and $\tan\beta_2$ denote the tangent value of the main influence angle of the downhill and the uphill, respectively. S_3 and S_4

denote the inflection offset distances of the left and right boundaries, respectively, and S_1 and S_2 denote the inflection offset distances of the downhill and uphill. θ is the propagation angle of the mining influence, and α is the dip angle of the coal seam. (see Figure 3(c))

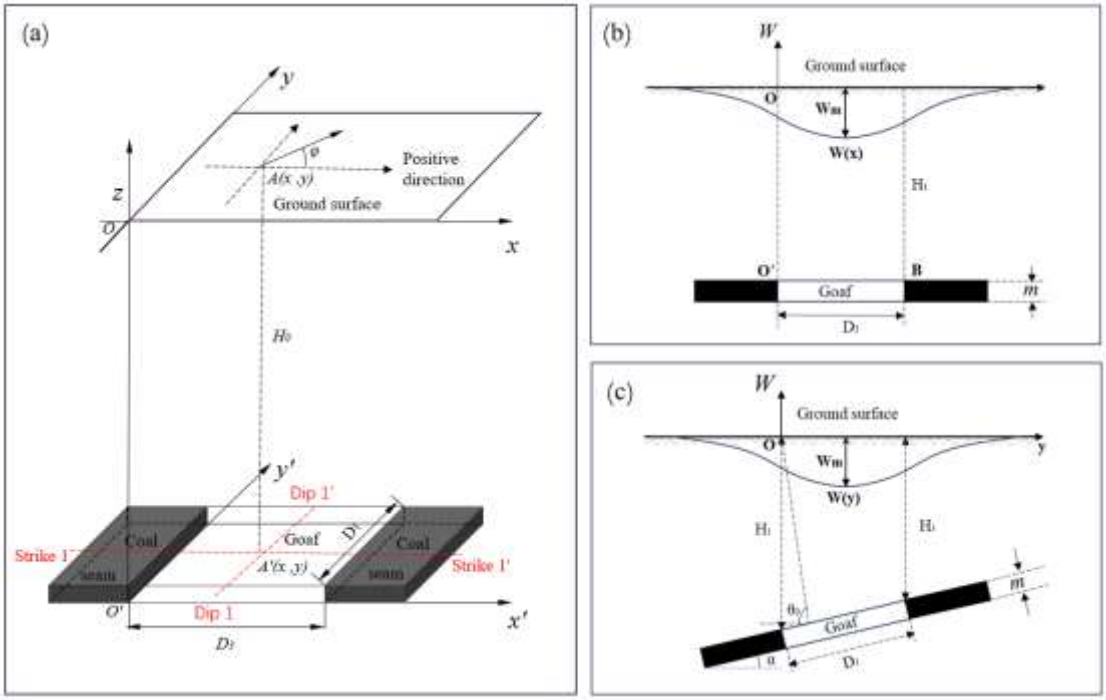

Figure 3. (a) Three-dimensional coordinate system of PIM; (b) Profiles of major cross-section along strike direction (profile Strike 1-1') ;(c) Profiles of major cross section along dip direction (profile Dip 1-1').

3.2. Horizontal movement due to mining in relation to surface tilting

According to Assumption 3 of the PIM, and based on the principles of elasticity, it is assumed that the total volumetric strain of the rock mass is zero.

$$\varepsilon_x + \varepsilon_z = 0 \tag{8}$$

The linear strains ε_x and $\varepsilon_z$along the x and z axes, respectively, are given by the principles of elasticity and considering the assumptions of the random media model. Thus, we have:

$$\varepsilon_x = \frac{\partial U(x,z)}{\partial x} \tag{9}$$

$$\varepsilon_z = -\frac{\partial W(x,z)}{\partial z} \tag{10}$$

In the Eq., $U(x,z)$ represents the horizontal displacement at point (x,z) within the rock layer due to the influence of mining. The negative sign in ε_z is due to the opposite directions of the W-axis and the Z-axis. Combining Eq. (8), (9), and (10):

$$\frac{\partial W(x,z)}{\partial z} = \frac{\partial U(x,z)}{\partial x} \tag{11}$$

The horizontal displacement $U(x,z)$ at the surface caused by mining a unit cell can be determined by integrating Eq. (11).

$$U(x,z) = \int \frac{\partial W(x,z)}{\partial x} dx + c(z) \tag{12}$$

Considering the symmetry of the model and the mining unit, the horizontal displacement at all points on the z-axis is zero, which implies that $c(z) = 0$. Therefore, we have:

$$U(x,z) = B(z)\frac{\partial W(x,z)}{\partial x} \tag{13}$$

Eq. (13) indicates that, according to the random media theory model, the horizontal displacement is proportional to the tilt, with the proportionality constant being constant for the same mining depth z. For a coal seam with a mining depth H, $B(z)$ is given by:

$$B(H) = b \cdot r = b\frac{H}{tan\,\beta} \tag{14}$$

where b is the horizontal movement coefficient, r is the radius of main influence. Further derivation from the unit mining subsidence basin and horizontal movement expressions shows that when the horizontal coal seam is mined to a limited extent, a proportional relationship still exists between the surface horizontal movement and surface dip on the strike and dip main fractures, that is,

$$U(x) = b\frac{H}{tan\,\beta} \cdot i(x) \tag{15}$$

$$U(y) = b\frac{H}{tan\,\beta} \cdot i(y) \tag{16}$$

Where $U(x)$ and $U(y)$ denote the horizontal movement of the surface along the strike and dip. $i(x)$ and $i(y)$ denote the dip of the surface along the strike and dip, respectively.

3.3. Three-Dimensional Deformation Monitoring in Mining Areas

As shown in Figure 4, a small portion of the image element array for DInSAR is assumed. Assuming that ΔN and ΔE are the sizes of the pixel along the north-south and east-west directions, respectively, i.e., the resolution size of the LOS deformation map obtained after geocoding to the WGS84 coordinate system. For the image element(x, y), it is tilted along the strike and dip, respectively:

$$i_E(x,y) = \frac{W(x+1,y) - W(x,y)}{\Delta E} \tag{17}$$

$$i_N(x,y) = \frac{W(x,y+1) - W(x,y)}{\Delta N} \tag{18}$$

Therefore, the surface horizontal displacements along the strike and dip main fractures can be expressed as:

$$U_E(x,y) = \frac{b \cdot H \cdot W(x+1,y) - W(x,y)}{\Delta E \cdot tan\,\beta} \tag{19}$$

$$U_N(x,y) = \frac{b \cdot H \cdot W(x,y+1) - W(x,y)}{\Delta N \cdot tan\,\beta} \tag{20}$$

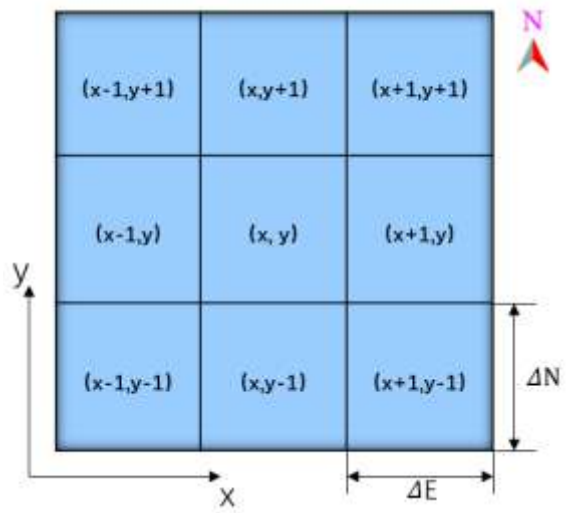

Figure 4. Pixel arrangement diagram of SAR images.

4. DATA PROCESSING AND RESULT ANALYSIS

4.1. InSAR Deformation Monitoring in Mining Area

Based on the differential interferometry scheme outlined in Table 1, differential interferometry was conducted on five SAR image datasets to produce four sets of differential interferograms. By integrating external DEM data, these image pairs were processed using SARscape 5.6 software. Accurate orbital data were applied to each set of differential interferograms to correct for errors caused by satellite orbit. The final results were obtained after DInSAR processing (see Figure 5(a)). DInSAR monitoring values for each observation point were extracted and compared with leveling data. The comparison results are presented in Figure 5(b) and 5(c).

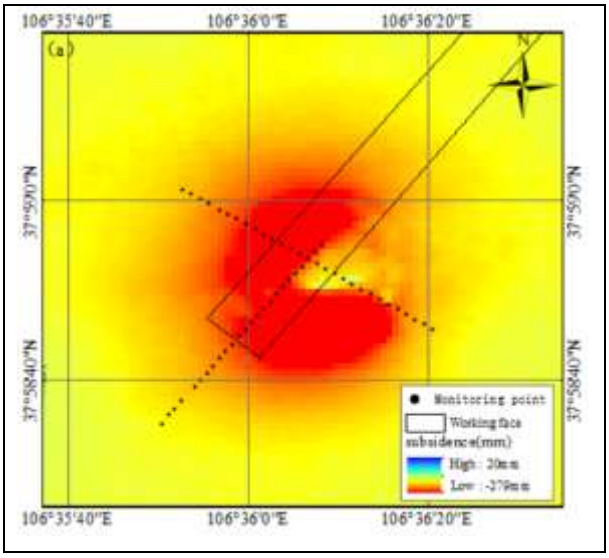

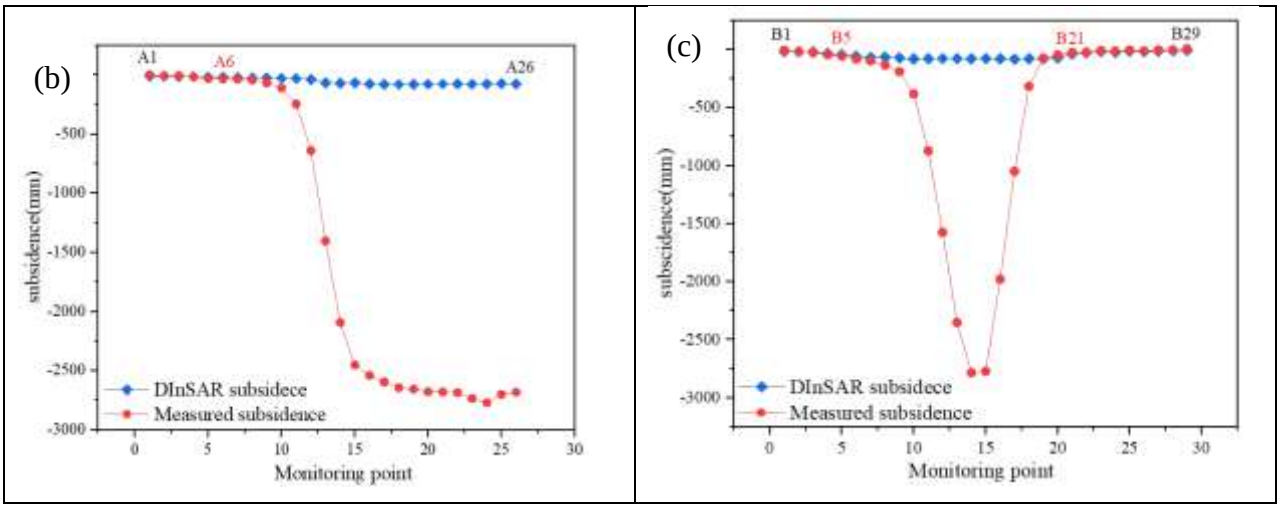

Figure 5. (a) Overlaid result map of DInSAR、(b) Comparison of DInSAR Monitoring and Leveling Data along the Strike Line、(c) Comparison of DInSAR Monitoring and Leveling Data along the Dip Line.

The results indicate a strong consistency between the DInSAR measurements and leveling data in regions of low-gradient deformation along the strike observation line A1-A6, as well as the dip observation lines B1-B5 and B21-B29. However, the ability to monitor large-gradient subsidence at the centre of subsidence is obviously insufficient.

4.2. Mine Area PIM Deformation Monitoring

Combining the leveling points with the Probability Integral Model (PIM) and using surface fitting methods, the PIM parameters for the mine area are inverted as $_{\mathrm{B}} = [q; \tan\beta; S_1; S_2; S_3; S_4; \theta; \mathrm{b}] = [2.1; 2.6; 91; 16; 8; 24; 86^{\circ}; 0.2]$ Substituting these parameters into Eq.s (4), (5), (6), and (7), the probability integral prediction basin for the 120101 working face in the mine is calculated, as shown in Figure 6(a).

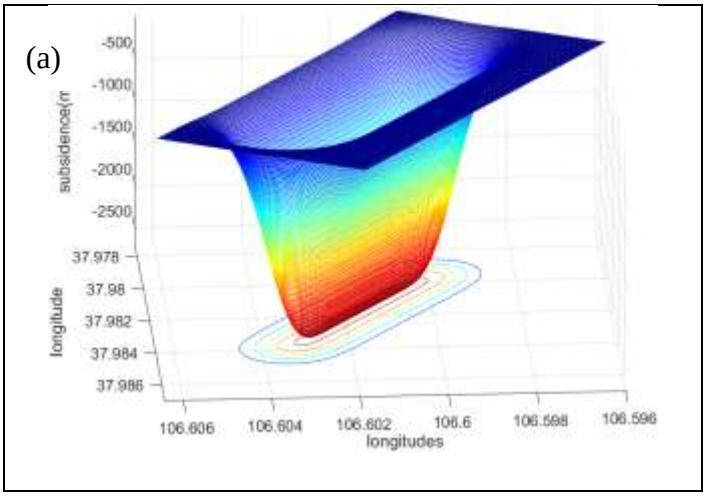

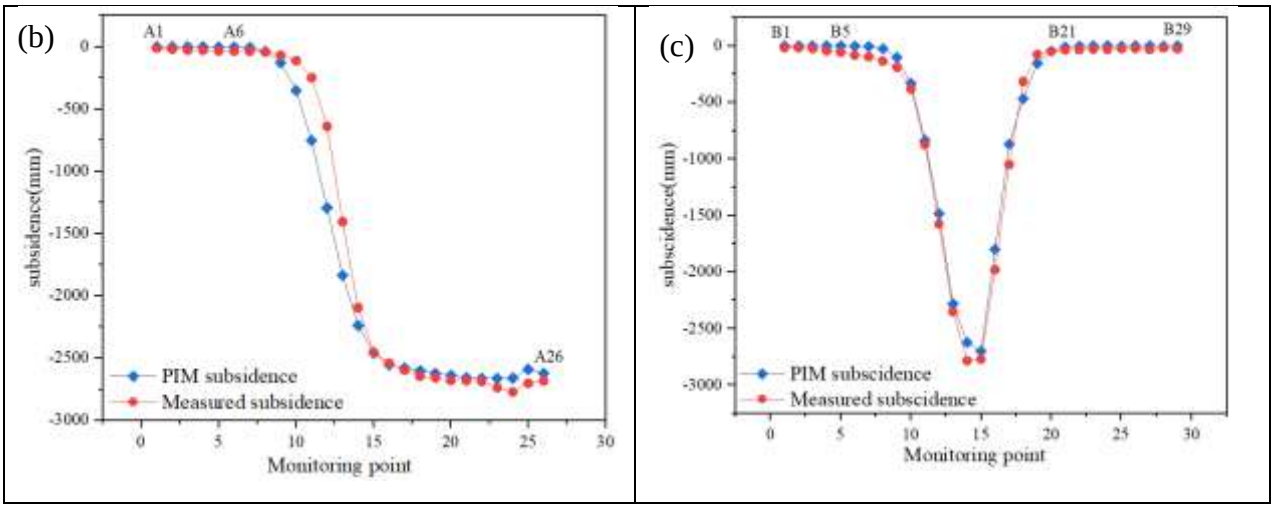

Figure 6. (a) Predicted Basin by PIM;(b) Comparison of PIM Monitoring and Leveling Data along the Strike Line;(c) Comparison of PIM Monitoring and Leveling Data along the Dip Line.

As shown in Figure 6(a), PIM detected a pronounced funnel-shaped subsidence basin above the 120101 working face, with a maximum subsidence of 2698 mm, indicating that PIM can effectively monitor significant subsidence. Comparing the subsidence data obtained from PIM with leveling data in Figure 6(b) and 6(c), it was found that the accuracy is higher near the maximum subsidence value, but the method shows larger errors at the edges of the working face.

4.3. Integrated Method for Extracting the Complete Surface Subsidence Basin of the Mining Area

InSAR is capable of accurately capturing the edge information of subsidence. PIM offers high monitoring accuracy at the core of the subsidence basin. By integrating the subsidence monitoring strengths of InSAR and PIM, one can acquire precise and comprehensive data on surface subsidence in mining regions. Based on deformation gradients and considering the resolution of Sentinel-1A imagery, which is 20m ×20m, the maximum detectable deformation gradient $d_{\max\ |InSAR}$ for N interferograms can be calculated as follows:

$$d_{max\ |InSAR} = \mu * D_{max} * N \tag{21}$$

According to the InSAR monitoring results, the average coherence coefficient is calculated to be $\gamma = 0.52$. Under this coherence condition, using Eq. (3) and (21), the maximum deformation detectable by InSAR is calculated to be 35 mm. A threshold of 35 mm is set for integrating the InSAR and probabilistic integral method subsidence results. When the subsidence is less than 35 mm, the InSAR monitoring value is used as the final subsidence result; when the subsidence exceeds 35 mm, the PIM monitoring value is used as the final subsidence result. This integration of InSAR and PIM provides a comprehensive subsidence basin map of the mining area. as shown in Figure. 7.

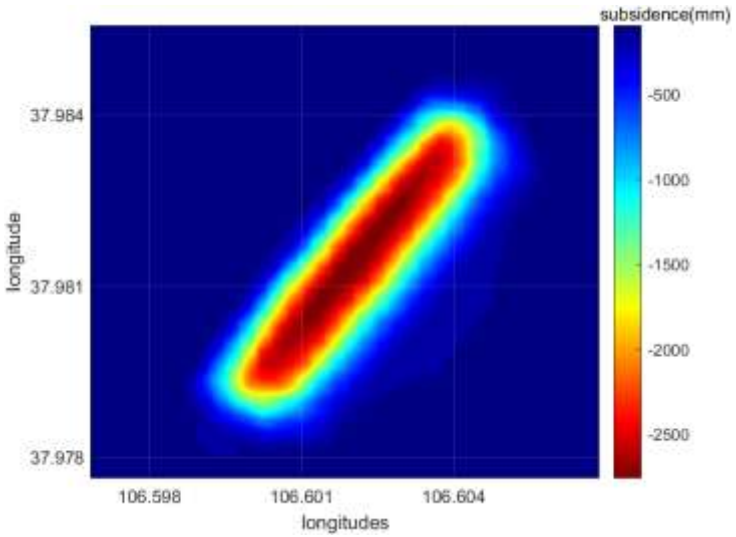

Figure 7. Subsidence results after the fusion of InSAR and PIM.

Figure 7 shows that by integrating the data from InSAR and the probabilistic integral method, a complete subsidence result for the mining area can be obtained. However, discontinuities appear at the fusion boundaries. To address this issue, a blending buffer zone is established on both sides of the fusion boundary to perform weighted averaging.

Based on the InSAR monitoring results and calculations using Eq. (3) and (21), the maximum deformation detectable by InSAR is 35 mm. This InSAR monitoring value will be used as the final subsidence result, with this value serving as the lower threshold for weighted averaging.

For the probabilistic integral method, the inflection point commonly manifests at the boundary along the principal axis of the subsidence basin, where the curvature of the subsidence curve transitions to zero. Combining the subsidence results predicted by PIM with the leveling and dip observation results, we determined that the 639 mm predicted by PIM serves as the upper critical threshold for the weighted average. When the subsidence exceeds 639 mm. The subsidence value derived from the probabilistic integral method is employed as the definitive outcome.

The final subsidence results were determined by weighted averaging the subsidence values predicted by InSAR and the probabilistic integral method when the subsidence was between 35 mm and 639 mm. Initially, 14 leveling points with subsidence amounts between 35 mm and 639 mm were selected. The differences between the InSAR monitoring results and the leveling measurements, and between the probabilistic integral method results and the leveling measurements, were calculated along with the mean squared errors of these differences. The calculated mean squared errors were 167 mm and 232 mm.

$$P_{InSAR} = \frac{\sigma_{PIM}^2}{\sigma_{InSAR}^2 + \sigma_{PIM}^2} = 0.42 \tag{22}$$

$$P_{PIM} = \frac{\sigma_{InSAR}^2}{\sigma_{InSAR}^2 + \sigma_{PIM}^2} = 0.58 \tag{23}$$

Based on Eq.s (22) and (23), the calculated values are $P_{PIM} = 0.42$ and $P_{InSAR} = 0.58$. Thus, by:

$$d = \begin{cases} d_{InSAR} & \mathrm{d} < 35\mathrm{mm} \\ 0.58d_{InSAR} + 0.42d_{PIM} & 35\mathrm{mm} \leq \mathrm{d} \leq 639\mathrm{mm} \\ d_{PIM} & \mathrm{d} > 639\mathrm{mm} \end{cases} \tag{24}$$

The complete mine subsidence basin after weighted averaging is obtained, as shown in Figure. 10. The d in Eq. (24) represents the final subsidence value.

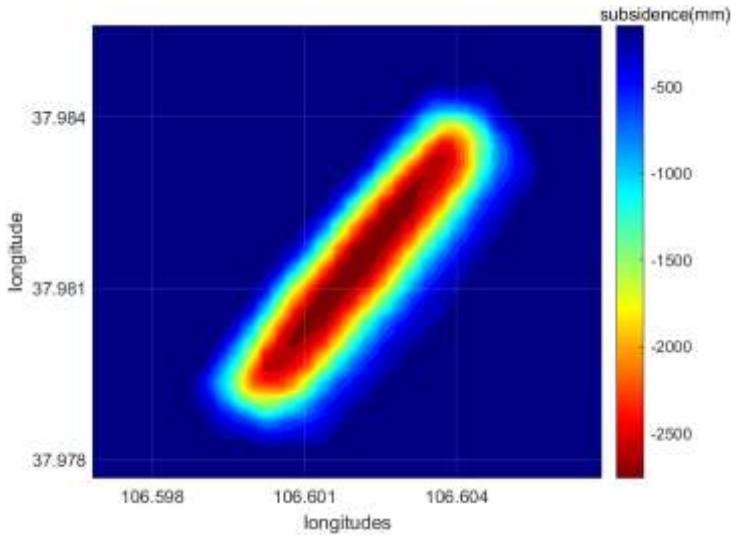

Figure 8. Settlement monitoring results after weighted fusion.

Figure 8 shows the weighted fused subsidence monitoring results. By integrating InSAR and PIM with weighted averaging, the issue of discontinuities at the fusion boundaries is resolved. Figure 9(a) and 9(b) show the comparison of the weighted fusion data for the strike and dip lines with the measured data, respectively. The RMSE of the fused subsidence data compared to the leveling data is 45.8. This indicates a closer match to the leveling data, resulting in improved monitoring accuracy.

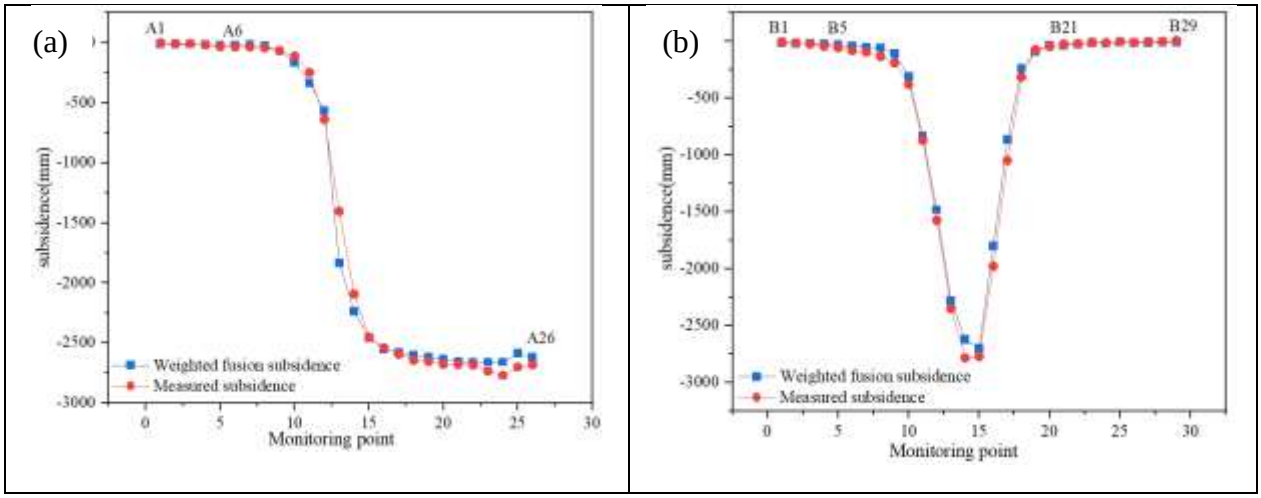

Figure 9. (a) Comparison between trendline-weighted fused data and leveling data; (b) Comparison between inclination line-weighted fused data and leveling data.

4.4. Results Analysis

To address the three-dimensional displacements caused by mine subsidence, the three-dimensional displacement of the mine area was extracted using the established model, as shown in Figures. 10(a), 10(c), and 10(e). The results of the calculations indicate that the maximum subsidence reaches approximately 2698 mm, occurring near the center of mining area. Additionally, the greatest displacement in the northward direction is around 1063 mm, while the maximum eastward displacement measures approximately 1669 mm.

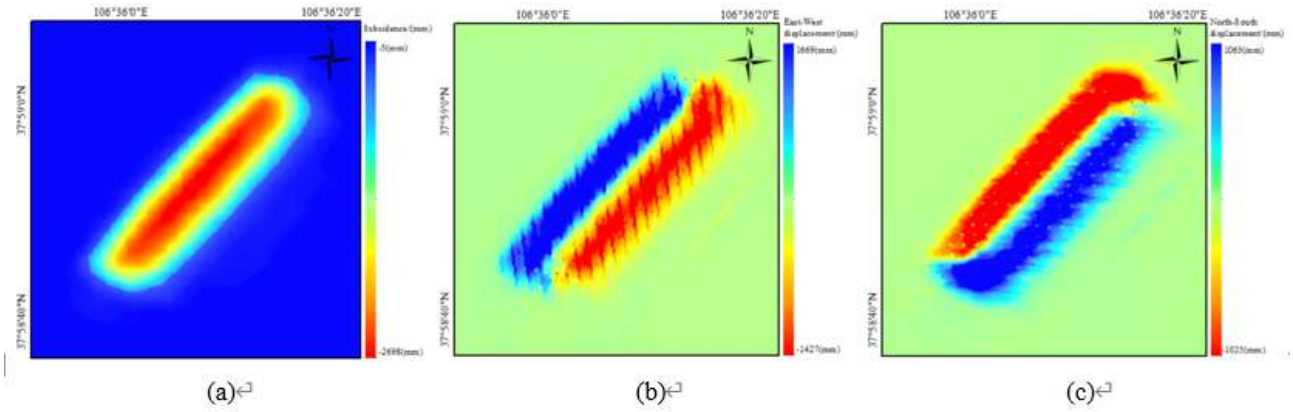

Figure 10. Vertical, east-west, north-south displacement

In order to further verify the accuracy of each method, the accuracy of the extracted InSAR+PIM, PIM and InSAR was evaluated using the monitoring points on the two observation lines. As shown in Table 1.

Table 1. Error analysis.

Methods	Edge Subsidence Area (A1~A6, B1~B5, B21~B29) RMSE/mm	Weighted Fusion Area (A7~A12,B6~B10, B18~L20) RMSE/mm	Overall Results RMSE/mm
InSAR	15.6	144.6	970.8
PIM	28.7	92.6	77.6
InSAR+PIM	10.6	65.6	45.8

1) Edge subsidence area: The PIM prediction model converges too quickly in the edge subsidence area, resulting in unsatisfactory prediction results. The RMSE between the subsidence value extracted by PIM and the leveling data is 28.7 mm; the RMSE between the InSAR monitoring results and the leveling data is 15.6 mm; the RMSE between the subsidence value obtained by data fusion of the two methods and the leveling data is 10.6; compared with InSAR and PIM, the monitoring accuracy is improved by 32% and 63%, respectively.
2) Weighted fusion area: In the weighted fusion area, the InSAR surface deformation information gradually weakens, while the PIM prediction result is higher than the leveling measurement value. After weighted fusion of the two data, the RMSE is 65.6 mm. Compared with InSAR and PIM, the monitoring accuracy is improved by 55% and 29%, respectively.
3) Overall results: The overall monitoring accuracy RMSE is 45.8 mm, which is 95% and 41% higher than InSAR and PIM, respectively.

5. DISCUSSION

5.1. Comparison with InSAR and PIM monitoring techniques

Advantages of InSAR Monitoring: InSAR technology offers all-weather, all-day monitoring capabilities and can cover extensive spatial areas. Compared to traditional point measurement techniques, InSAR is more efficient in monitoring large-scale surface subsidence, particularly excelling in scenarios with small gradient subsidence. Limitations: InSAR has significant limitations when dealing with large gradient subsidence caused by coal mining. When large gradient deformation occurs on the surface, it can lead to image decorrelation, resulting in inaccurate deformation information.

Advantages of PIM Monitoring: PIM can partially address the issue of image decorrelation in InSAR when monitoring large gradient subsidence. It can overcome phase loss issues caused by large gradient subsidence to some extent without requiring additional auxiliary observation data. This makes PIM cost-effective, particularly suitable for monitoring scenarios with limited resources.Limitations: Although PIM can compensate for InSAR's shortcomings, it suffers from rapid convergence, which prevents it from accurately capturing subsidence in edge regions. Additionally, the effectiveness of PIM depends on the accuracy of the model, and it may not be precise in extracting large gradient deformation in complex terrain or coal layers.

The research proposes a comprehensive method combining InSAR, the PIM, and the log-logistic model. Advantages: This method successfully overcomes the limitations of traditional InSAR technology in monitoring large gradient deformation and the technical issue of PIM's inability to accurately capture edge subsidence. Limitations: The accuracy of the subsidence basin center obtained through PIM calculations still needs improvement.

5.2. Comparison with existing 3D deformation models for mining subsidence

In recent years, many studies have utilized InSAR technology to extract three-dimensional deformation information from mining areas by employing SAR images from various orbits, including ascending and descending, and combining these with InSAR-based mining subsidence models. These methods primarily use technologies such as InSAR, MAI, and offset tracking to capture surface deformation in different directions, which is then decomposed into vertical, east-west, and north-south components. Although widely used, these techniques are independent of mining subsidence modeling and have limitations, including the need for SAR images from multiple orbits, which increases monitoring costs, and difficulties in acquiring surface subsidence in areas with significant deformation.

This paper proposes a strategy that combines the mining subsidence model with InSAR, utilizing mining subsidence PIM as prior information to address three-dimensional deformation in mining areas through single-track InSAR. Screening and consistency tests on the monitoring data validate that the results are highly correlated with measured leveling data and exhibit improved accuracy compared to using DInSAR or PIM alone. The advantages of this model include reduced monitoring costs due to the use of single-pass InSAR information, However, its limitations include applicability solely to horizontal or nearly horizontal coal seams, rendering it unsuitable for inclined or steeply dipping seams.

5.3. Improvement of large gradient surface deformation monitoring methods in mining areas and future research prospects

Tackling the complexities inherent in monitoring significant-gradient surface deformations within mining environments, this paper proposes a new method combining InSAR, probabilistic integration method (PIM) and log- logistic model, which is designed to address the shortcomings of traditional monitoring techniques in capturing large-scale three-dimensional deformation. This approach aims to overcome the limitations of traditional monitoring techniques in capturing large-scale three-dimensional deformations. Compared to conventional leveling and RTK technologies, this method not only provides higher spatial coverage and accuracy but also significantly reduces labor intensity and costs. By leveraging the strengths of PIM and InSAR technologies, this method demonstrates excellent adaptability in handling large-gradient deformations. Specifically, it effectively addresses continuity issues in transition areas between subsidence edges and centers through a weighted fusion strategy, solving challenges that traditional methods struggle to handle.

Despite the progress made with the proposed method, future research must address its limitations. For instance, improving the method's adaptability under varying geological conditions and further optimizing the PIM model to reduce reliance on data accuracy are critical areas for future

investigation. Additionally, exploring the integration of other high-precision three-dimensional monitoring technologies, such as 3D laser scanning and UAVs, with the proposed method could potentially lead to breakthroughs in monitoring surface deformation in mining areas. Therefore, future research should not only focus on refining existing methods but also on exploring innovative solutions to enhance the efficiency and reliability of mining safety monitoring.

6. CONCLUSION

In view of the limitations of InSAR and PIM in 3D mining subsidence monitoring, this paper proposes a new 3D deformation monitoring method that integrates InSAR, InSAR and log-logistic model to obtain the 3D deformation of the subsidence basin. The method was applied to the 120101 working face of Yangchangwan Coal Mine, and the effectiveness of the method was verified by using Sentinel-1A images and leveling data. The results show that:

1) For the subsidence basin obtained by the proposed method, the root mean square error (RMSE) between the calculated subsidence value and the measured value in the edge area is 10.6 mm, which is 32% and 63% higher than the monitoring accuracy of InSAR and PIM, respectively; in the weighted fusion area, the RMSE is 65.6 mm, which is 55% and 29% higher than the accuracy of InSAR and PIM, respectively. The overall RMSE is 45.8 mm, which is 95% and 41% higher than that of InSAR and PIM, respectively.

2) The maximum vertical displacement, east-west displacement and north-south displacement calculated by this method are 2698 mm, 1669 mm and 1063 mm, respectively. The results show that this method can obtain high-precision three-dimensional deformation data and has the potential for practical engineering applications.

REFERENCE

[1] Fan, H.D., Gao, X.X., Yang, J.K., Deng, K.Z., et al, 2015. Monitoring Mining Subsidence Using A Combination of Phase-Stacking and Offset-Tracking Methods. *Remote Sens.* 7, 9166-9183. https://doi.org/10.3390/rs70709166

[2] Bell, F., Stacey, T., Genske, D., 2000. Mining subsidence and its effect on the environment: some differing examples. Environmental Geology .40, 135–152. https://doi.org/10.1007/s002540000140

[3] Sahoo, S., Khaoash, S., 2020.Impact assessment of coal mining on groundwater chemistry and its quality from Brajrajnagar coal mining area using indexing models. Journal of Geochemical Exploration. 215, 106559. https://doi.org/10.1016/j.gexplo.2020.106559.

[4] Chen, H.Y., Zhao, C.Y., Tomás, R., Chen, L.Q., et al., 2023. Retrieving the Kinematic Process of Repeated-Mining-Induced Landslides by Fusing SAR/InSAR Displacement, Logistic Model, and Probability Integral Method. Remote Sens. 15, 3145. https://doi.org/10.3390/rs15123145

[5] Yan, W., Chen, Z., Chen, J., Zhao, C.,2024. Spatiotemporal Patterns of Vegetation Evolution in a Deep Coal Mining Subsidence Area: A Remote Sensing Study of LiangBei, China. Remote Sens. 16, 3204. https://doi.org/10.3390/rs16173204

[6] Jiang, K., Yang, K., Zhang, Y., Li, Y., et al., 2023. An Extraction Method for Large Gradient Three-Dimensional Displacements of Mining Areas Using Single-Track InSAR, Boltzmann Function, and Subsidence Characteristics. Remote Sens. 15, 2946. https://doi.org/10.3390/rs15112946

[7] Chaussard, E., Amelung, F., Abidin, H., Hong, H.S.,2013. Sinking cities in Indonesia: ALOS PALSAR detects rapid subsidence due to groundwater and gas extraction. Remote Sens. 128, 150-161. https://doi.org/10.1016/j.rse.2012.10.015.

[8] Hu, B.L., Chen, L., Zou, Y.F., Wu, X.X., et al., 2021.Methods for Monitoring Fast and Large Gradient Subsidence in Coal Mining Areas Using SAR Images: A Review. *IEEE Access*. 9, 159018-159035. https://doi.org10.1109/ACCESS.2021.3126787

[9] Luo, H.B., Li, Z.H., Chen, J.J., Pearson, C., et al., 2019. Integration of range split spectrum interferometry and conventional InSAR to monitor large gradient surface displacements. Int. J. Appl. Earth Obs. Geoinf. 74, 130–137. https://doi.org/10.1016/j.jag.2018.09.004.

[10] Imamoglu, M., Balik Sanli, F., Cakir, Z. et al., 2022. Rapid ground subsidence in the Küçük Menderes Graben (W. Turkey) captured by Sentinel-1 SAR data. Environ Earth Sci .81, 221. https://doi.org/10.1007/s12665-022-10339-3

[11] Li, Z.W., Yang, Z.F., Zhu, J.J., H, J., et al., 2015. Retrieving three-dimensional displacement fields of mining areas from a single InSAR pair. J Geod. 89,17–32. https://doi.org/10.1007/s00190-014-0757-1

[12] Fuhrmann, T., Garthwaite, M.C., 2019. Resolving Three-Dimensional Surface Motion with InSAR: Constraints from Multi-Geometry Data Fusion. Remote Sens. 11, 241. https://doi.org/10.3390/rs11030241

[13] Zhu, J.J., Li, Z.W., Hu, J., 2017. Research progress and methods of InSAR for deformation monitoring. Acta Geod Cartogr Sinica. 46,1717–1733. https://doi.org/10.11947/J.AGCS.2017.20170350

[14] Yang, Z., Li, Z., Zhu, J., Feng, G., et al., 2018. Deriving time-series three-dimensional displacements of mining areas from a single-geometry InSAR dataset. J. Geod. 92, 529–544. https://doi.org/10.1007/s00190-017-1079-x

[15] Jo, Min-Jeong, Jung, H.S., Chae, S.H., 2018.Advances in Three-Dimensional Deformation Mapping from Satellite Radar Observations: Application to the 2003 Bam Earthquake. Geomatics. Natural Hazards and Risk. 9 ,678–690. https://doi.org/10.1080/19475705.2018.1473293

[16] Suhadha, A.G., Harintaka, H., 2024. Multidimensional displacement analysis of Semeru Volcano, Indonesia following December 2021 eruption from multitrack InSAR observation. Earth Sci Inform.17, 1539–1552 https://doi.org/10.1007/s12145-024-01248-z

[17] Zheng, M.N., Deng, K.Z., Fan, H.D., H, J.L., 2019. Monitoring and analysis of mining 3D deformation by multi-platform SAR images with the probability integral method. Front. Earth Sci.13,169–179. https://doi.org/10.1007/s11707-018-0703-2.

[18] Yang, Z.F., Zhu, J.J., Xie, J., Li, Z.W., et al., 2022.Resolving 3-D Mining Displacements From Multi-Track InSAR by Incorporating With a Prior Model: The Dynamic Changes and Adaptive Estimation of the Model Parameters. IEEE Trans. Geosci. Remote Sens. 60, 1–10. https://doi.org/10.1109/TGRS.2021.3093058

[19] Mastro, P., Serio, C., Masiello, G., Pepe, A., 2020. The Multiple Aperture SAR Interferometry (MAI) Technique for the Detection of Large Ground Displacement Dynamics: An Overview. Remote Sens. 12, 1189. https://doi.org/10.3390/rs12071189

[20] Yang, Z., Li, Z., Zhu, J., Preusse, A., et al., 2018. An Alternative Method for Estimating 3-D Large Displacements of Mining Areas from a Single SAR Amplitude Pair Using Offset Tracking. IEEE Trans. Geosci. Remote Sens. 56, 3645–3656. https://doi.org/10.1109/TGRS.2018.2803285

[21] Ou, D., Tan, K., Du, Q., Chen, Y., et al., 2018. Decision Fusion of D-InSAR and Pixel Offset Tracking for Coal Mining Deformation Monitoring. Remote Sens. 10, 1055. https://doi.org/10.3390/rs1007105

[22] Hu, J., Li, Z.W., Ding, X.L., Zhu, J.J., et al., 2013. Derivation of 3-D coseismic surface displacement fields for the 2011 Mw 9.0 Tohoku-Oki earthquake from InSAR and GPS measurements. Geophys. J. Int. 192, 573–585. https://doi.org/10.1093/gji/ggs033

[23] Liu, C.J., Ji, L.Y., Zhu, L.Y., Xu, C.J., et al., 2024. Interseismic strain rate distribution model of the Altyn Tagh Fault constrained by InSAR and GPS. Earth and Planetary Science Letters.642,118884. https://doi.org/10.1016/j.epsl.2024.118884.

[24] Wang, H., Wright, T. J., Z, J.L., P, L.C., 2019. Strain rate distribution in south-central Tibet from two decades of InSAR and GPS. Geophys. Res. Lett. 46, 5170-5179. https://doi.org/10.1029/2019GL08191

[25] Li, Z.W., Yang, Z.F., Zhu, J.J., Hu, J., et al., 2015. Retrieving three-dimensional displacement fields of mining areas from a single InSAR pair. J. Geod .89, 17–32. https://doi.org/10.1007/s00190-014-0757-1

[26] Selvakumaran, S., Rossi, C., Marinoni, A., Webb, G., et al., 2020. Combined InSAR and Terrestrial Structural Monitoring of Bridges. IEEE Trans. Geosci. Remote Sens.58, 7141-7153. https://doi.org/10.1109/TGRS.2020.2979961.

[27] Wang, Z.H., Dai, H.Y., Yan, Y.G., Liu, J.B., et al., 2023. Combination of InSAR with a Depression Angle Model for 3D Deformation Monitoring in Mining Areas. Remote Sens. 15,1834. https://doi.org/10.3390/rs15071834

[28] Yang, Z.F., Li, Z.W., Zhu, J.J., Hu, J., et al., 2016. InSAR-Based Model Parameter Estimation of Probability Integral Method and Its Application for Predicting Mining-Induced Horizontal and Vertical Displacements. IEEE Trans. Geosci. Remote Sens. 54, 4818–4832. https://doi.org/10.1109/TGRS.2016.2551779

[29] Wang, R., Wu, K., He, Q.M., He, Y.B., et al., 2022.A Novel Method of Monitoring Surface Subsidence Law Based on Probability Integral Model Combined with Active and Passive Remote Sensing Data. Remote Sens. 14, 299. https://doi.org/10.3390/rs14020299

[30] Wang, L.Y., Deng, K.Z., Fan, H.D., Zhou, F.Q., 2018. Monitoring of large-scale deformation in mining areas using sub-band InSAR and the probability integral fusion method. Int. J. Remote Sens. 40, 2602–2622. https://doi.org/10.1080/01431161.2018.1528403IF

[31] Massonnet, D., Feigl, K.L., 1998. Radar interferometry and its application to changes in the Earth's surface. Rev. Geophys. 36, 441–500. https://doi.org/10.1029/97RG03139

[32] Baran, I., Stewart, M., Claessens, S., 2005. A new functional model for determining minimum and maximum detectable deformation gradient resolved by satellite radar interferometry. IEEE Trans. Geosci. Remote Sens. 43, 675–682. https://doi.org/10.1109/TGRS.2004.843187

[33] Dai, S.H., Zhang, Z.J., Li, Z., Liu, X.G., et al., 2023. Prediction of Mining-Induced 3-D Deformation by Integrating Single-Orbit SBAS-InSAR, GNSS, and Log-Logistic Model (LL-SIG). IEEE Trans. Geosci. Remote Sens. 31, 1-13. https://doi.org/10.1109/TGRS.2023.3334735

[34] Yang, Z., Li, Z., Zhu, J., Yi, H., et al., 2017. Deriving Dynamic Subsidence of Coal Mining Areas Using InSAR and Logistic Model. Remote Sens. 9, 125. https://doi.org/10.3390/rs9020125